

**FINAL PROJECT REPORT**  
**AFOSR Grant FA9950-06-0112**

**U.S. AIR FORCE OFFICE OF SCIENTIFIC RESEARCH**  
**ATTN: Dr. David S. Stargel.**  
**Program Manager, Structural Mechanics**  
**AFOSR/RSA**  
**875 North Randolph Street**  
**Suite 325, Room 3112**  
**Arlington, VA 22203**

**PENETRATION PHYSICS AT THE MESO-SCALE**

*By*

*C. W. Felice and Y. M. Gupta*

**Institute for Shock Physics**  
**Applied Science Laboratory**  
**Pullman, WA 99164-2816**  
**Phone: 509-358-7700**  
**Email: [cfelice@wsu.edu](mailto:cfelice@wsu.edu)**

**October 6, 2009**

**20091231166**

REPORT DOCUMENTATION PAGE					Form Approved OMB No. 0704-0188	
The public reporting burden for this collection of information is estimated to average 1 hour per response, including the time for reviewing instructions, searching existing data sources, gathering and maintaining the data needed, and completing and reviewing the collection of information. Send comments regarding this burden estimate or any other aspect of this collection of information, including suggestions for reducing the burden, to Department of Defense, Washington Headquarters Services, Directorate for Information Operations and Reports (0704-0188), 1215 Jefferson Davis Highway, Suite 1204, Arlington, VA 22202-4302. Respondents should be aware that notwithstanding any other provision of law, no person shall be subject to any penalty for failing to comply with a collection of information if it does not display a currently valid OMB control number.						
PLEASE DO NOT RETURN YOUR FORM TO THE ABOVE ADDRESS.						
1. REPORT DATE (DD-MM-YYYY) 06-10-2009		2. REPORT TYPE Final Report			3. DATES COVERED (From - To) 2/15/06-5/31/09	
4. TITLE AND SUBTITLE Penetration Physics at the Meso-Scale				5a. CONTRACT NUMBER NA		
				5b. GRANT NUMBER FA9550-06-1-0112		
				5c. PROGRAM ELEMENT NUMBER NA		
				5d. PROJECT NUMBER NA		
6. AUTHOR(S) Conrad W. Felice and Y. M. Gupta				5e. TASK NUMBER NA		
				5f. WORK UNIT NUMBER NA		
7. PERFORMING ORGANIZATION NAME(S) AND ADDRESS(ES) Washington State University Institute for Shock Physics PO Box 642816 Pullman, WA 99164-2816				B. PERFORMING ORGANIZATION REPORT NUMBER FA9550-06-1-0112 Final		
9. SPONSORING/MONITORING AGENCY NAME(S) AND ADDRESS(ES) US Air Force, AFRL AF Office of Scientific Research 875 N Randolph Street, Room 3112 Arlington, VA 22203 Dr. Stargel/RSA				10. SPONSOR/MONITOR'S ACRONYM(S) AFOSR		
				11. SPONSOR/MONITOR'S REPORT NUMBER(S) AFRL-SR-AR-TR-09-0373		
12. DISTRIBUTION/AVAILABILITY STATEMENT DISTRIBUTION A: Approved for Public Release.						
13. SUPPLEMENTARY NOTES Any opinions, findings, and conclusions or recommendations expressed in this publication are those of the author and do not necessarily reflect the views of the Air Force.						
14. ABSTRACT This effort focused on understanding the underlying physics through a multi-scale computational approach to quantify penetrator performance into particulate geologic materials at impact velocities up to 1,500 m/sec. The computational approach employed an explicit, updated Lagrangian finite element formulation that performed 2-D plain strain and axisymmetric analyses of multi-body systems subjected to shock wave loading. To capture the particulate response, a simple elastic-plastic constitutive model was used to represent the discretized grain behavior while relying on a parallel processing computing platform to capture the evolution of the penetrator/media interaction. The penetrator was modeled as an elastic body. Computational results showed the affects of impact velocity on projectile stability/trajectory and the influence of intergranular friction. The influence of nose geometry on penetrator stability and trajectory was also modeled and quantified by tracking the resultant force vector on an ogive, cylindrical, and blunt nosed penetrator during penetration into a granular body with a 0.3 friction coefficient and 30 percent porosity.						
15. SUBJECT TERMS Penetration mechanics, granular media, impact velocity, friction, pososity						
16. SECURITY CLASSIFICATION OF:			17. LIMITATION OF ABSTRACT  U	18. NUMBER OF PAGES	19a. NAME OF RESPONSIBLE PERSON Conrad W. Felice	
a. REPORT  U	b. ABSTRACT  U	c. THIS PAGE  U			19b. TELEPHONE NUMBER (Include area code) (509) 358-7847	

## 1.0 INTRODUCTION

This effort focused on understanding the underlying physics through a multi-scale computational approach to quantify penetrator performance into particulate geologic materials at impact velocities up to 1,500 m/sec. The computational approach employed an explicit, updated Lagrangian finite element formulation that performed 2-D plain strain and axisymmetric analyses of multi-body systems subjected to shock wave loading. The approach was first used to capture intrinsic features observed during shock experiments on aluminum that were only able to be quantified through an analysis at the grain level. For application to particulate geologic media, the analysis procedure was modified to include the effects of grain size distribution, porosity, and intergranular friction. To capture the particulate response, a simple elastic-plastic constitutive model was used to represent the discretized grain behavior while relying on a parallel processing computing platform to capture the evolution of the penetrator/media interaction. The penetrator was modeled as an elastic body. Computational results showed the affects of impact velocity on projectile stability/trajectory and the influence of intergranular friction. The influence of nose geometry on penetrator stability and trajectory was also modeled and quantified by tracking the resultant force vector on an ogive, cylindrical, and blunt nosed penetrator during penetration into a granular body with a 0.3 friction coefficient and 30 percent porosity.

Following this introduction, Section 2.0 of this report will review the initial project objectives their evolution. Accomplishments and new findings are presented in Section 3.0. Section 4.0 lists the personnel involved in the effort followed by a list of publications and interactions that resulted during the award period.

## 2.0 OBJECTIVES, EVOLUTION AND INTERACTION WITH AF PERSONNEL

The goal of this research was to understand the underlying physics of penetrator mechanics into particulate materials at high impact velocity employing a meso-scale computational approach. The specific objectives of the effort were as follows.

- Quantify the penetrator impact velocity initiating instability at three nose geometries and corresponding length to diameter ratios (2D).
- Introduction of thermal effects specifically to identify interface mechanisms governing the penetrator particulate media interaction (2D).
- Investigate and identify dominate meso-scale phenomena that can be best represented in a continuum scale computation.
- Extend the code ISP-TROT to 3D.

The meso-scale computations were performed by modifying the ISP-TROT computer code developed in-house at the Institute for Shock Physics. ISP-TROT is an explicit, updated Lagrangian finite element that performs 2-D plain strain and axisymmetric analysis of multi-

---



body system subjected to shock wave loading. It is based on the SRI code TROT in terms of the calculation of incremental strains and stresses.

During the investigation, the focus of the effort concentrated principally on the first objective and examining combinations of particulate material conditions, penetrator material and nose geometry to identify the transition velocity and the dominant interaction mechanisms that contribute to an unstable trajectory. This evolution occurred as a result of communication with AFRL project personnel at Eglin AFB and the Program Manager, Dr. Victor Giurgiutiu. Additionally, two focused workshops that the PIs participated in on Particulate Mechanics hosted by Dr. William Cooper also greatly influenced the direction of the effort.

### 3.0 ACCOMPLISHMENTS/NEW FINDINGS

#### Mesoscale simulations

A schematic view of the 2D plane strain mesoscale simulation procedure is shown in Fig. 1. The sand particulate system was generated by the in-house program ISP-SAND [1], and is based on an energy minimization technique and a modified Voronoi tessellation [2, 3]. ISP-SAND generates 2D polyhedron shaped grains based on various inputs including mean grain size, uniform or normal size distribution, and porosity. Samples of different sand geometries considered in the simulations are shown in Fig. 2. Fig. 2a shows grains of 60  $\mu\text{m}$  uniform size with 30% porosity. Figures 2b and 2c show grains with 60  $\mu\text{m}$  mean grain size,  $\pm 30\%$  uniform size distribution, 30% porosity, and with two different mesoscale features. The grains in Fig. 2b were generated with a more uniform distribution of porosity than the grains in Fig. 2c giving rise to more clustered grains in Fig. 2c. The shape of the simulated 2D grains was compared to actual sand grains [4, 5] and found to compare reasonably well. Porosity was generated by mixing porosity designated grains of size 70% of the actual mean grain size. These smaller porosity grains were removed in the last stage of the particulate system generation to create porosity in the form of individual pores or a number of pores clustered together as shown in Figs. 1 and 2. The penetrator was an ogive nose projectile of CRH 3.5, 3.85, and length 1.6 mm. The spatial discretization of the sand grains and projectile into 10  $\mu\text{m}$  constant strain triangles was carried using the program Cubit 9.1 [6]. Further preprocessing was done by the code ISP-PREP [7] that assigned initial conditions, boundary conditions, and other parameters needed for simulation.

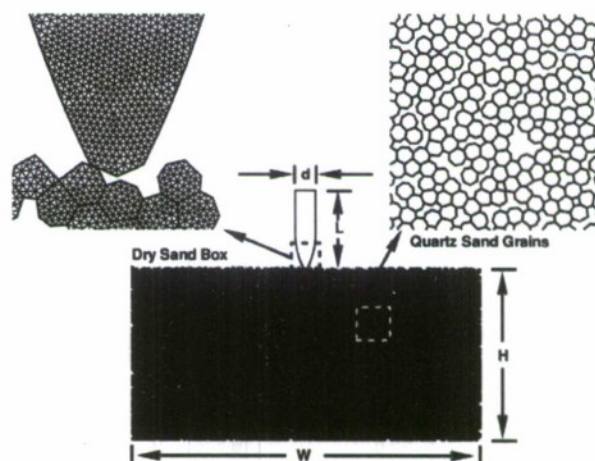


Fig. 1: Schematic view of the 2D mesoscale simulation approach with ogive nose projectile penetrating a sand target with individual sand grains and heterogeneities modeled explicitly.

The 2D plane strain mesoscale simulations were carried out using an updated Lagrangian parallel finite element code ISP-TROTP [8,9]. As with most wave propagation simulations, the program temporally simulates the penetration event by integrating the governing equations using an explicit time marching scheme. The deformation of individual sand grains, projectile, and interactions between them are analyzed at every time step, forming the core of the present approach. As mentioned earlier, thermal effects and material failure during penetration were not incorporated in this study. Hence, the erosion, melting, and disintegration of the projectile and fragmentation of the sand particles were not considered in the present work.

To the best of our knowledge, the material response of individual sand grains under shock compression is not known. As such, each grain was simulated as a z-cut quartz particle whose shock induced elastic-inelastic deformation was modeled using a non-linear elastic model [10] along with an overstress model incorporating a mean stress dependent inelastic threshold stress [12]. The projectile material was taken to be steel whose shock response was modeled using a non-linear elastic model [11] and a simplified bilinear von-Mises flow strength model. The material models and relevant parameters for the sand grains and steel projectile are presented in Table 1.

The interactions between sand grains and between grains and the projectile were analyzed at each time step using the contact algorithm developed earlier [8]. The coincident edges of sand grains seen in Figs. 1 and 2 are the consequence of the Voronoi tessellation, which may or may not be present in-situ. These coincident edges were free to slide and had relative displacements from the beginning of the impact loading. Simulations were carried out for normal projectile impacts for 0.5, 1.0, and 1.5 km/s impact velocities. Experiments have shown projectile instability to occur prior to one full projectile length of penetration [13]. For this reason, simulations at each impact velocity were carried out for one full projectile length of penetration. The full length penetration was considered to occur when the top of the projectile had reached approximately the initial top level of the sand. Details of the various simulations, discussed in the next section, are summarized in Table 2.

We note that no rigorous approach was adopted to establish the scaling from the laboratory experimental dimensions to the dimensions chosen in the present simulations. The dimensions were chosen iteratively to minimize the computing time. The sand body dimensions in all the simulations, except the last two, were  $W$  (width) = 7.1 mm and  $H$  (height) = 3.5 mm. The deep

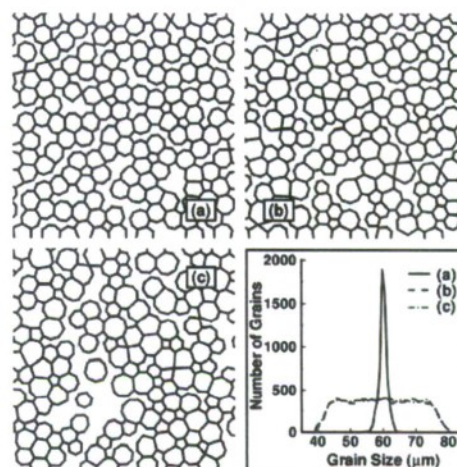


Fig. 2: Sand grains generated as regular polyhedrons: (a) 60  $\mu\text{m}$  uniform grain size, (b) 60  $\mu\text{m}$  mean grain size with  $\pm 30\%$  uniform size distribution placed uniformly, (c) same as b, but placed randomly giving pronounced clustered grains.



Table 1: Material properties used in the simulations.

Non-linear Elastic Model and Parameters used for Sand Grains and Steel Projectile	
<b><u>Sand Grains<sup>26</sup>:</u></b>	<b><u>Steel Projectile<sup>27</sup>:</u></b>
${}^0\rho = 2648.5 \text{ kg/m}^3$	${}^0\rho = 7823.0 \text{ kg/m}^3$
$G = 46.92 + 1.873 P + 0.3459P^2 \geq 46.92 \text{ GPa}$	$G = 77.5 \text{ GPa}$
$P = P_H \left(1 - \frac{\gamma\mu}{2}\right) + \frac{\gamma E}{V}$ ; $\mu = \frac{P}{{}^0\rho} - 1$ ; $\gamma\rho = {}^0\gamma {}^0\rho$	$P_H = 163.9\mu + 294.3\mu^2 + 500.0\mu^3$ ; ${}^0\gamma = 1.1\epsilon$
$P_H = 43.19\mu + 156.2\mu^2 + 48.6\mu^3$ ; ${}^0\gamma = 0.675$	
${}^0\rho$ is the initial density, $G$ is the shear modulus, $P$ is the negative of mean stress, $\mu$ is the volume compression, ${}^0\gamma$ is the initial Mie-Gruneisen constant, $E$ is the specific internal energy, and $V$ is the specific volume.	
Inelastic Model for the Sand Grains and Steel Projectile	
<b><u>Overstress Model for Sand Grains<sup>28</sup>:</u></b>	<b><u>von-Mises Model for Steel Projectile:</u></b>
$s_{ij} = s_{ij}^T \left[ 1 - \left( \frac{\sqrt{3J_2'}}{\tau_y} \right) \frac{\Delta t}{T_R} \right]$ ; $J_2' = \frac{1}{2} s_{ij} s_{ij}$	$\bar{\sigma} = \sqrt{3J_2'} \leq 1.16 + 0.12\bar{\epsilon}^p$ ; $d\bar{\epsilon}^p = \sqrt{\frac{2}{3}} d\epsilon_{ij}^p d\epsilon_{ij}^p$
$\tau_y = \begin{cases} 2.353 + 0.667P & 0 \leq P \leq 3.067 \text{ GPa} \\ 4.4 & P > 3.067 \text{ GPa} \end{cases}$ ; $T_R = 3.5 \text{ ns}$	
$s_{ij}$ are the deviatoric stresses, $J_2'$ is the second invariant of the deviatoric stresses, $\tau_y$ is the mean stress dependent flow strength, $\Delta t$ is the incremental time step, $T_R$ is the relaxation time, $\bar{\sigma}$ is the effective stress, $\bar{\epsilon}^p$ is the effective plastic strain, and $d\epsilon_{ij}^p$ are the incremental plastic strains.	

penetration simulations in the last two runs of Table 2 were carried out with  $H = 7.1 \text{ mm}$  for the sand body. In our simulations, the number of grains varied from 1502 to 12307, number of finite element nodes varied from 223K to 521K, and number of finite elements varied from 336K to 777K. The chosen simulations dimensions are scaled down approximately 17 times from laboratory experiments on bullets penetrating coarse sand grains of 1 mm in size.

Table 2. Summary of simulations with parameter values and final center-of-mass X- displacement.

Run No	Sand Grains			Projectile			Friction
	Mean <sup>1</sup> Size ( $\mu\text{m}$ )	Placement <sup>2</sup>	Type	Velocity (km/s)	Type	Center-of-Mass X- Displacement (mm)	
1	60	U (1)	1	0.5	1	0.0053	0.3
2	60	U (1)	1	1.0	1	0.0008	0.3
3	60	U (1)	1	1.5	1	0.0055	0.3
4	60	U (1)	1	1.5	E	0.0054	0.3
5	60	U (1)	E	1.5	1	0.0062	0.3
6	60	U (1)	E	1.5	E	0.0013	0.3
7	60	U (1)	1	1.5	E	0.0157	0.3
8	120	U (1)	1	1.5	E	0.0176	0.3
9	60	U (2)	1	1.5	E	0.0035	0.3
10	60	U (3)	1	1.5	E	0.0020	0.3
11	60	U (4)	1	1.5	E	0.0045	0.3
12	60	U (5)	1	1.5	E	0.0039	0.3
13	60	C (1)	1	1.5	E	0.0147	0.3
14	60	U (1)	1	1.5	E	0.0012	0.3
15	60	U (1)	1	1.5	1	0.0035	0.0
16	60	U (1)	1	1.5	E	0.0001	0.0
17	60	U (1)	E	1.5	E	0.0106	0.0
18	60	U (1)	E	1.5	E	0.0290	0.3

The present simulations were carried out in parallel using the shared memory parallel machine Altix-4700. The machine has a total of 64 blades. Each blade has 2 dual cores 1.6 GHz Itanium2 Montecito processors and 8 GB memory. The resulting 256 processor nodes machine with 0.512 TB shared memory, NUMalink3 interconnect, and 1.4 TB disk space is operational with Intel compiler suites and PBSPro software. Each of the present simulations utilized 16 to 32 nodes (number of nodes was kept fixed during each simulation) and required a wall clock time of 3 to 10 days.

Projectile instability was quantified and compared with self-consistent variables of lateral (X-direction) displacement of the projectile's center of mass and rotational momentum about the center-of-mass. The final lateral displacement for each simulation is presented in Table 2. A finite value of the lateral displacement indicates that the projectile experienced unbalanced lateral forces, which was consistent with the rotational momentum. The rotational momentum was the moment of momentum about the center-of-mass of the projectile, i.e.,  $RM = \sum r_i \times m_i v_i$  where  $RM$  denotes the rotational momentum,  $r_i$  is the position vector from center of mass to node  $i$ ,  $m$  is the mass,  $v$  is the velocity vector of the node, and the summation is carried over all the projectile nodes. The finite value of the rotational momentum also indicates change in path of the projectile from the vertical. The two variables were consistent with the average forces applied on the projectile in the lateral direction. The closer this average is to zero the more stable the penetration event.

### Penetration results

Fig. 3 shows the penetration features at the end of the simulations for three impact velocities (Runs 1-3) using the contours for von-Mises effective stress  $\bar{\sigma} = \sqrt{3J'_2}$ , where  $J'_2$  is the second invariant of the deviatoric stress tensor. The center dashed-dot line represents the initial vertical direction of penetration. The simulation at 1.0 km/s stopped before reaching one full length of penetration. The mushrooming (lateral spread of the projectile nose) due to the inelastic

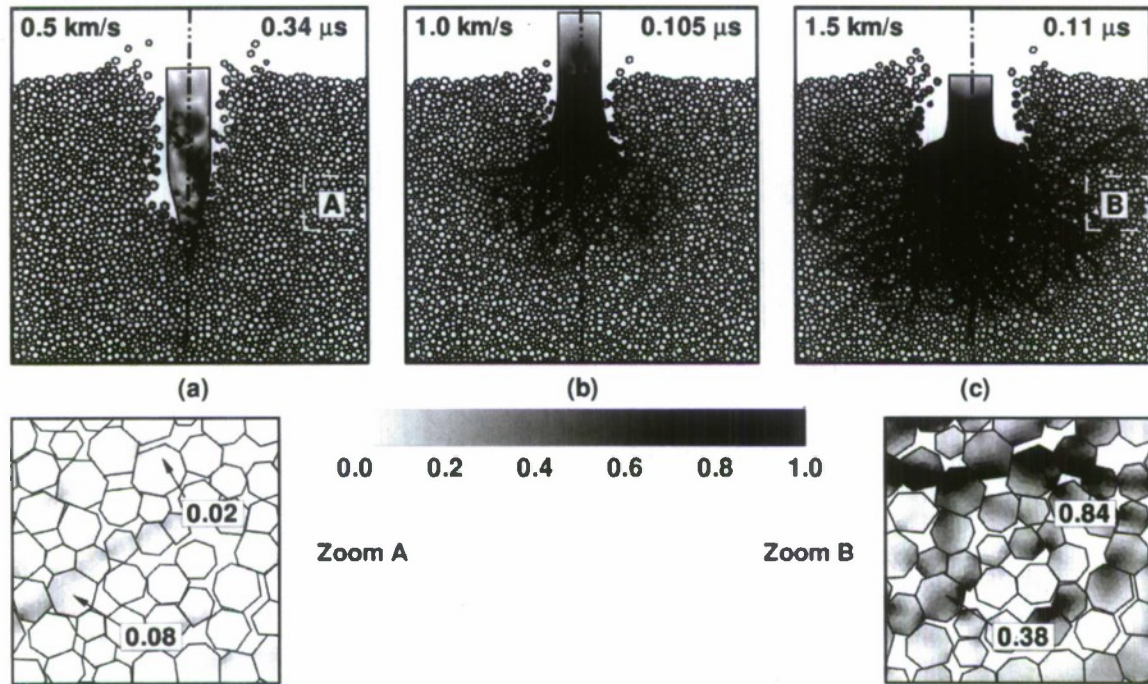


Fig. 3: Penetration features with contours of the von-Mises stress  $\bar{\sigma}$  at one full length penetration at 0.5, 1.0, and 1.5 km/s impact velocities (Runs 1-3) with zoomed views at the end of the penetration zone. The simulation at 1.0 km/s terminated abnormally.



deformation in the projectile is negligible at 0.5 km/s, but becomes visible at 1.0 km/s and considerable at 1.5 km/s. The resulting increase in the load bearing area of the projectile reduces the depth-of-penetration despite the increase in the impact velocity. Also, the mushrooming is not symmetric, indicating that the sand grains exert an inhomogeneous load.

An important aspect of the simulations is the prediction of stress fingers or force chains shown in Fig. 3. Stress fingers seen in granular materials [13] are caused by individual grains impacting the next grain in line and transmitting stresses. It is observed that the deformation zone in the sand is independent of the impact velocity. The simulations at 1.0 km/s terminated early and the final deformation zone was small. But, the extent of the deformation zone was similar for one full length penetration at 0.5 km/s and 1.5 km/s impact velocities. The stresses inside the deformation zone at 1.5 km/s are, as expected, higher than at 0.5 km/s impact velocity seen in the enlarged views of Fig. 3 zoomed at the same locations towards the end of the penetration zone.

The temporal variations of the rotational momentum are shown in Fig. 4 for the three impact velocities. At the lowest velocity, the rotational momentum is not significant and oscillates close to zero. At 1.0 km/s, it gains magnitude and shows an increasing trend in the negative direction before the simulation terminated. At 1.5 km/s, the rotational momentum increases monotonically in the negative direction.

The corresponding variations of the X- direction force and momentum of the projectile shown in Fig. 5 are consistent with the calculated rotational momentum. The forces and momentum oscillates around zero at the 0.5 km/s impact velocity. They have oscillatory but finite value at 1.5 km/s impact velocity. These results indicate that the projectile instability should increase with impact velocity and a change in trajectory should be visible at 1.5 km/s impact velocity. However, the trajectory change is not appreciable and lateral displacement of the center-of-mass of the projectile is same for the two impact velocities. This result likely indicates that the finite values of the rotational momentum, lateral force, and lateral momentum at 1.5 km/s are due to the asymmetric mushrooming and inhomogeneous flow of the material in the lateral direction, not due to the instability as was expected.

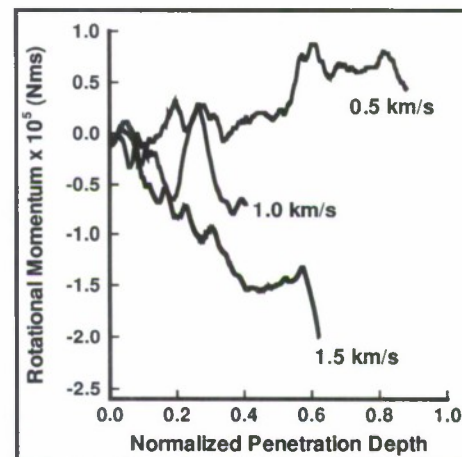


Fig. 4: Rotational momentum of the inelastic projectile at the three impact velocities shown in Fig. 3 (Runs 1-3).

#### **Effect of increasing sand grains and projectile stiffness**

The inelastic deformation causing projectile mushrooming (that inhibited the penetration) and excessive deformation of sand grains under the penetrator may not be realistic. A stiffer projectile material will allow its nose shape to be preserved to maximize the penetration. The sand grains will likely fragment and retain their granular characteristics with reduced size rather

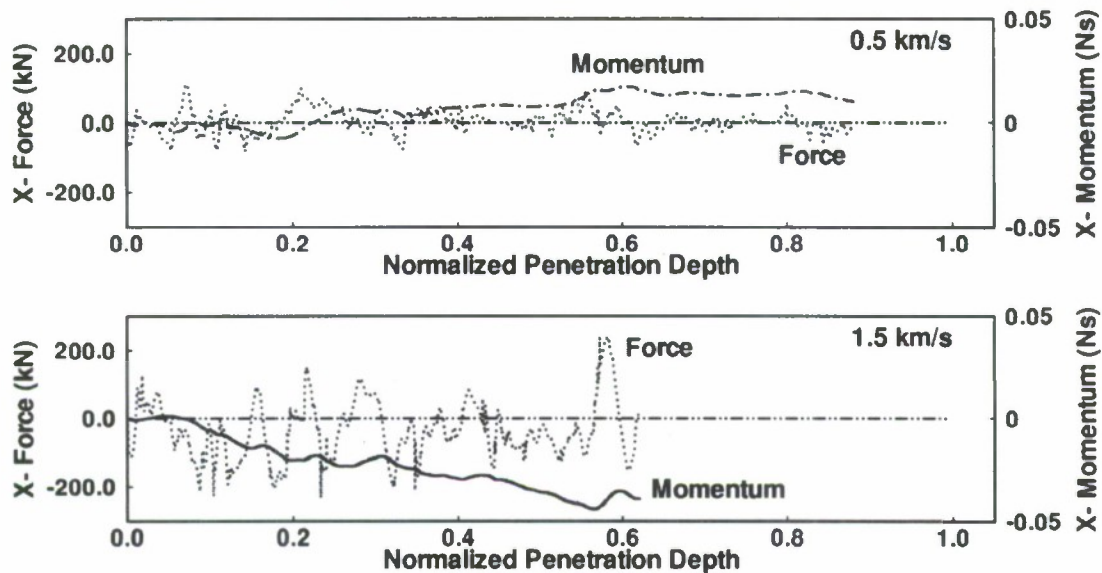


Fig. 5: Lateral (X- direction) force exerted on and lateral momentum gained by the inelastic projectile during penetration at 0.5 km/s and 1.5 km/s shown in Fig. 3 (Runs 1, 3).

than being squeezed to flaky shapes. To incorporate these phenomena without modeling failure and fragmentation, simulations were carried out (Runs 4-6) that preserved the projectile nose and sand grain shapes by assuming the materials to be elastic

Fig. 6 shows the full-length penetration at 1.5 km/s impact velocity for three cases: (a) elastic projectile and inelastic grains, (b) inelastic projectile and elastic grains, and (c) elastic projectile and elastic grains. As before, the inelastic projectile in Fig. 6b has lower depth-of-penetration due to mushrooming. The elastic grains distribute the load more evenly which facilitates penetration compared to the inelastic grains of Fig. 3. This feature allows deeper penetration by the elastic projectile as seen in Fig. 6c. However, the penetration of elastic projectile into inelastic grains of Fig. 6a has distinctively different features. The sand grains deform and get lodged under the moving projectile nose creating the region of concentrated deformation under the projectile. The inhomogeneous resistance to penetration around the nose provided by the lodged grains cause tipping of the projectile, making it unstable.

The rotational momentum values for the three cases in Fig. 6 are shown in Fig. 7. The elastic projectile in inelastic sand grains is most unstable. The clear change in trajectory of the projectile in Fig. 6a correlates well with the high and increasing value of the rotational momentum in Fig. 7 indicating instability. The change in trajectory is evident in Fig. 6c along with the rotational momentum attaining a lower value. It may be inferred that realistic phenomena of inelastic deformation of grains followed by their fragmentation will lie somewhere between the cases (a) and (c). Nonetheless, the projectile that preserves the nose shape should become unstable at one full-length of penetration.



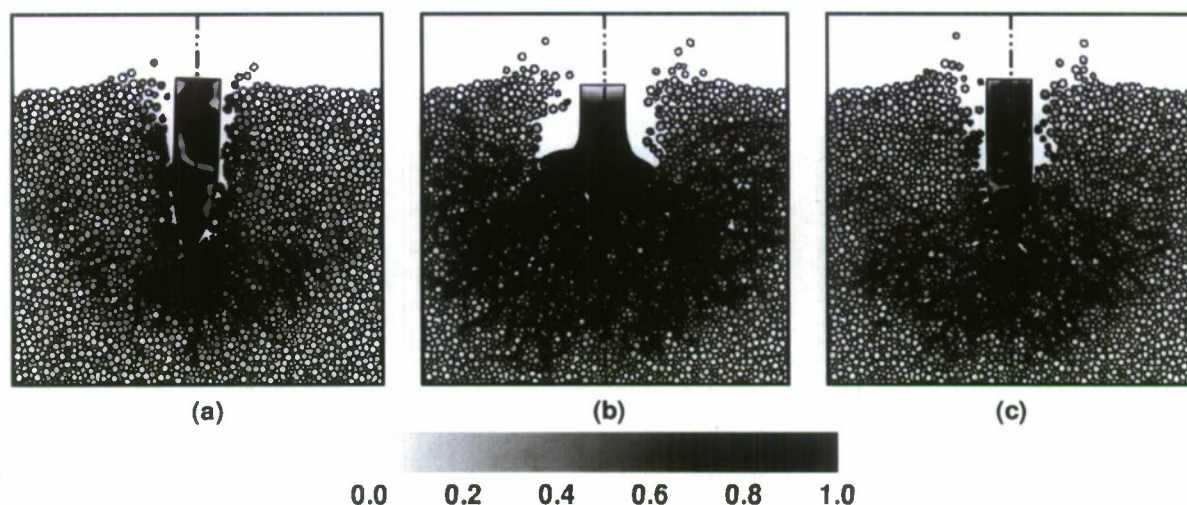


Fig. 6: Penetration features with contours of the von-Mises stress  $\bar{\sigma}$  showing effect of projectile and sand grain stiffness at 1.5 km/s impact velocity: (a) elastic projectile and inelastic sand grains, (b) inelastic projectile and elastic sand grains, and (c) elastic projectile and elastic sand grains (Runs 4-6).

#### Effect of grain size and grain size distribution

The elastic projectile penetration was simulated with 60  $\mu\text{m}$  uniform grain size (Run 7) and 120  $\mu\text{m}$  mean grain size having a  $\pm 30\%$  uniform size distribution (Run 8) at 1.5 km/s impact velocity, keeping all other parameters the same. Fig. 8 shows the full length penetration features for the two cases. Fig. 9 shows the rotational momentum values for the two cases along with the earlier case of 60  $\mu\text{m}$  mean grain size with  $\pm 30\%$  size distribution shown as 60D. The particulate system with uniform grains has less lateral motion as seen in Fig. 8 when compared to the distributed grains simulation shown in Fig. 6. This feature increases the load concentration directly under the projectile nose making the penetration zone narrower and deeper. The large cluster of grains under the nose is off-center and increases the rotational momentum (Fig. 9) and the center of mass displacement (Table 2). The increase in grain size increases the instability and changes in the trajectory. The 120  $\mu\text{m}$  mean grain size has similar rotational momentum, but higher center-of-mass displacement compared to the 60  $\mu\text{m}$  mean grain size. The amount of clustered grains and

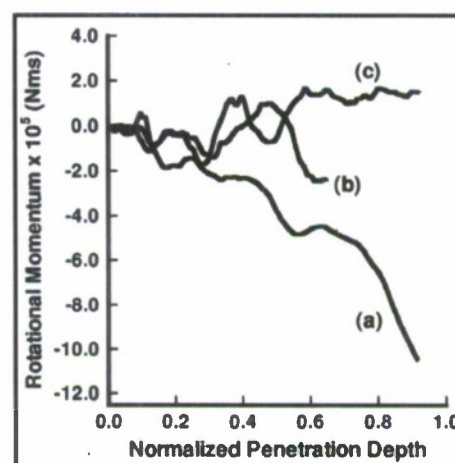


Fig. 7: Rotational Momentum of the elastic projectile for the three cases with varying stiffness of the projectile and sand grains (Runs 4-6).



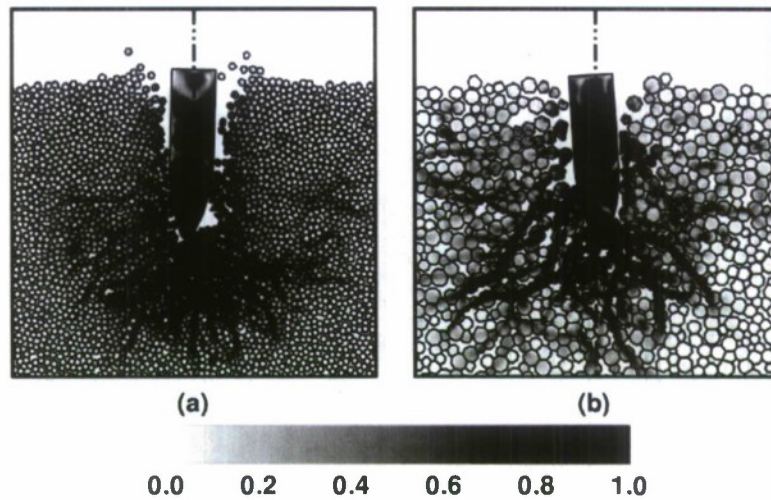


Fig. 8: Penetration features with contours of the von-Mises stress  $\bar{\sigma}$  showing effects of grain size and size distribution at 1.5 km/s impact velocity: (a) 60  $\mu\text{m}$  uniform grains (Run 7), and (b) 120  $\mu\text{m}$  mean grain size with  $\pm 30\%$  size variation (Run 8).

their inelastic deformation directly under the projectile are less for the bigger grains. We note that the sand system with larger grains was generated using an increased pore size (70% of the mean grain size). The increased instability for the larger grain size may, in part, be due to the larger pore size resulting into larger rigid body displacements.

#### Effect of random placement of sand grains

The sand particulate system in the above simulations was generated with the random seed of 1 in ISP-SAND. The simulations were carried out with four additional particulate systems generated by varying the random seed as 2, 3, 4, and 5 (Runs 9-12). The 60  $\mu\text{m}$  mean grain size and  $\pm 30\%$  uniform size distribution were unaltered in the generation. It was found that the one full length penetration state was very similar for the five different systems (not shown) with similar penetration zone, stress chains, and instability. The rotational momentum for the five different systems is compared in Fig. 10 and is marked as R1 to R5. The absolute value of the momentum is very similar showing similar instability and change in trajectory. ISP-SAND was then modified to randomly distribute the

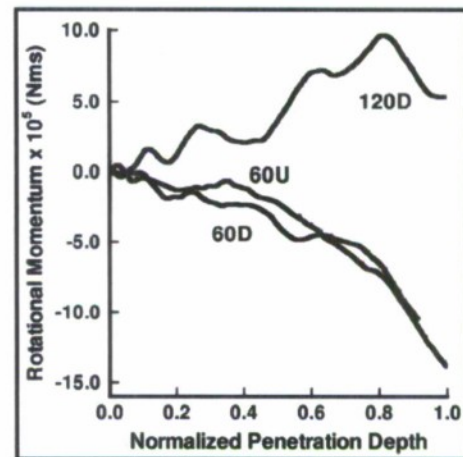


Fig. 9: Rotational Momentum of the elastic projectile at 1.5 km/s impact velocity: U indicates uniform grains and D indicates  $\pm 30\%$  uniform variation (Runs 4,7,8).

pores (instead of uniform distribution) while keeping the overall porosity the same. This change resulted in clustered grains and larger regions of empty space in the sand body as seen in Fig. 2c. The rotational momentum for this case is represented as C (Run 13) in Fig. 10. The instability increased with the randomly distributed porosity (more realistic physical situation) and clustered grains as compared to the uniformly distributed porosity.

### Effect of porosity

Simulations were carried out with 20% and 40% porosities for the 60  $\mu\text{m}$  mean grain size and  $\pm 30\%$  size distribution. The simulations with 20% porosity were not successful in most of the cases due to very large deformation of sand grains and, hence, are not reported here. The results from simulations with 40% porosity showed similar phenomena as discussed above. The inelastic impactor (not shown) mushroomed and had a reduced depth-of-penetration due to the larger load bearing area. But, an increase in porosity reduced the resistance to penetration that reduced mushrooming and resulted in an increased depth-of-penetration compared to the 30% porosity simulation. The reduced resistance to penetration at higher porosity increased the stability of the elastic projectile (Run 14). This is seen from the full-length penetration state shown in Fig. 11a compared to Fig. 6a. The lower wave speed and increased wave dispersion expected at higher porosity reduced the size of the penetration zone considerably with grain deformation concentrated closer to the projectile. The rotational momentum in Fig. 11b also shows that the projectile instability was reduced with an increase in porosity of the sand target.

### Effects of friction

The above cases were simulated with a friction coefficient of 0.3 between sand grains, and between sand grains and the projectile. To examine the effects of friction, penetrations of the inelastic and elastic projectiles (Runs 15, 16) were simulated for the frictionless case, i.e., setting

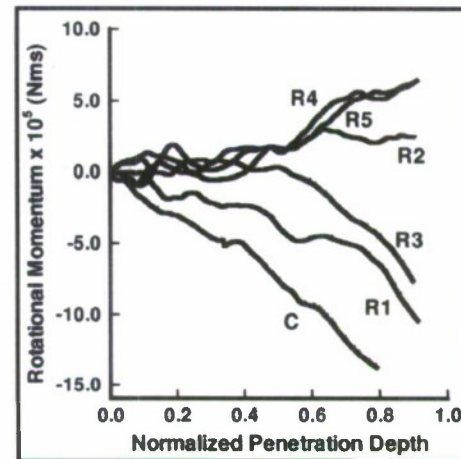


Fig. 10: Rotational Momentum of the elastic projectile at 1.5 km/s impact velocity showing effects of random placement of sand grains for same mean grain size and size distribution:

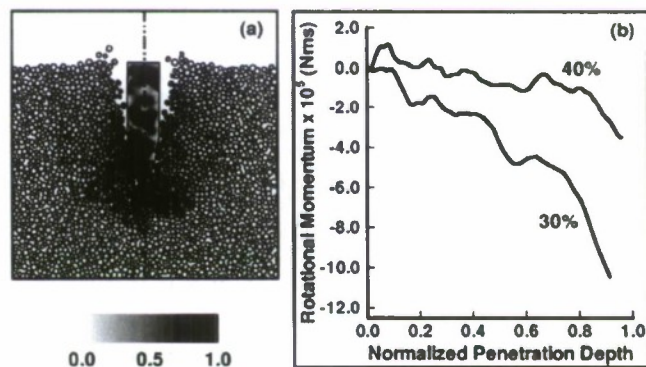


Fig. 11: (a) Penetration features with contours of the von-Mises stress  $\bar{\sigma}$  at 40% porosity (Run 14) and (b) rotational momentum for the two porosities (Runs 4, 14) showing the effect of porosity at 1.5 km/s impact velocity.



the friction coefficient to be zero. The results showed that removing friction reduced the resistance to penetration as the grains were able to slide without resistance. This increased the projectile stability as well as the depth-of-penetration. Moreover, the load exerted on the projectile was more symmetric as determined by the nearly symmetric mushrooming of the inelastic projectile (not shown). The increased stability is seen in the rotational momentum results in Fig. 12 for the friction and non-friction cases involving inelastic and elastic projectiles. The instability is at a maximum for the case of elastic projectile with friction.

### Deeper penetration simulation

The simulations discussed so far were carried out for one full projectile length of penetration. The instability was shown by the increasing rotational momentum coupled with the visual inspection of the projectile orientation at the full penetration length. The arguments in favor of the instability were consistent with the displacement of the center-of-mass of the projectile presented in Table 2, lateral force on the projectile, and rotational momentum of the projectile. Though the instability ensues at one full projectile length of penetration, the above simulations do not establish that the projectile in the most unstable case will continue to change the path. To explore this issue further, two simulations were carried out for 3 projectile lengths of penetration.

The height of the sand box was increased to 7.1 mm for the deeper penetration simulations. The enlarged sand body had over 12,000 grains and the number of triangular elements exceeded 700,000. The penetration of the elastic projectile was simulated with frictionless grains in the first case (Run 17) and with a 0.3 friction coefficient in the second case (Run 18). Because the computation time becomes a significant issue with simulations of this magnitude, the grains were considered elastic in both cases to circumvent the smaller time integration steps due to the inelastic deformation of grains. We recall that the elastic projectile was unstable at one body length of penetration for the case of elastic sand grains. The projectile state at 3 body lengths of penetration for the two cases is shown in Fig. 13 and the rotational momentum is shown in Fig. 14. Fig. 13 shows that the projectile was more unstable for the friction case. It changed orientation by almost 450 from the initial vertical direction. Rotational momentum plots in Fig. 14 show that with friction, the projectile slowly gains rotational momentum until it reaches a critical point and then turns abruptly. The projectile was unstable for the frictionless case as well, gaining the rotational momentum faster than the friction case. However, the penetration is more oscillatory. A large pull back toward the end of the simulations indicates that the projectile path

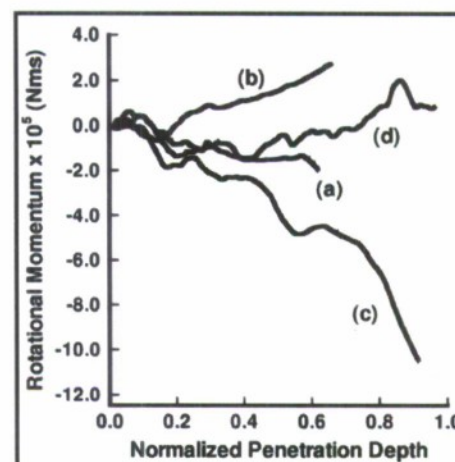


Fig. 12: Rotational Momentum showing effect of friction at 1.5 km/s impact velocity: (a) inelastic projectile and 0.3 friction (Run 3), (b) inelastic projectile and 0.0 friction (Run 15), (c) elastic projectile and 0.3 friction (Run 4), and (d) elastic projectile and 0.0 friction (Run 16).



may not deviate as much in the dry sand with lower friction. The final configuration in Fig. 13(a) is consistent with this finding.

### Summary

2D plane strain mesoscale simulations were carried out to gain insight into the instability and trajectory change of ogive nose projectiles penetrating dry sand. The dimensions of the projectile and the sand target were chosen iteratively to simulate the penetration with available computational resources. The sand target had a representative particulate system with 60  $\mu\text{m}$  and 120  $\mu\text{m}$  mean grain sizes, with or without  $\pm 30\%$  uniform size distribution, and 30% and 40% porosities distributed uniformly or randomly throughout the sand body. The simulations were carried out for a normal impact at velocities of 0.5 km/s, 1.0 km/s and 1.5 km/s. The deformation of the projectile and individual sand grains was analyzed using non-linear elastic and inelastic material models. The interactions between sand grains and between sand grains and the projectile were analyzed using a contact algorithm. A uniform constant coefficient of friction 0.3 was assumed in most simulations. Simulations were also carried out for the frictionless case. The instability was quantified and compared in terms of the displacement of the center-of-mass of the projectile, lateral force on the projectile, and rotational momentum of the projectile. The simulations were carried out for one projectile length of penetration. The instability was indicated by an appreciable displacement of the center-of-mass, and finite and increasing rotational momentum that also correlated with the visual trajectory change of the projectile. Finally, simulations for 3 body lengths of penetration were carried out to confirm that significant trajectory change for the projectile would occur if the instability ensued at one body length of penetration.

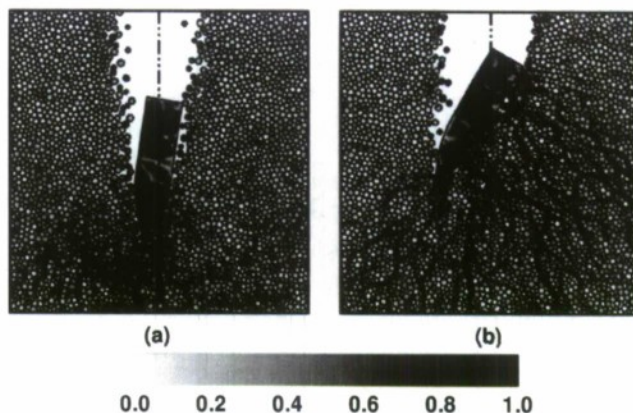


Fig. 13: Deeper penetration simulation results showing penetration features with contours of the von-Mises stress  $\bar{\sigma}$  at 3 full lengths of penetration for the case of elastic grains and 1.5 km/s impact velocity: (a) 0.0 friction, and (b) 0.3 friction (Runs 17, 18).

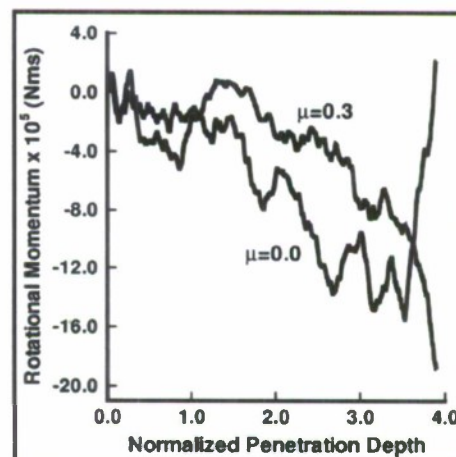


Fig. 14: Rotational Momentum of the elastic projectile from the deeper penetration simulation for the two cases of Fig. 13 (Runs 17, 18)

The principal finding of our work is that the mesoscale simulation approach, incorporating particulate heterogeneities and the response of individual sand grains, results in an inhomogeneous loading of the projectile that causes projectile instability and trajectory change during high velocity penetration. Our approach inherently predicted the stress chains or force chains that are assumed to govern the penetration and stability of the projectile. The instability invariably increased with the increase in impact velocity. The increased stability depicted by the mushroomed projectiles in our simulations is not realistic. The mushrooming, due to the large inelastic deformation, increased the load bearing area resulting in lower depth-of-penetration and increasing stability. In reality, the projectile will not mushroom either due to the material stiffness or due to the break up of the laterally mushroomed material. The elastic projectile simulated the former effect in the present work.

The present simulations showed that the instability was unaffected by the sand grains random arrangement as long as the mean grain size, size distribution, porosity, porosity distribution, etc. remained consistent. Projectile instability increased when uniform grains were incorporated, and with increased grain size and with random distribution in porosity that made the grains cluster together. The reduced lateral motion of the sand grains and increased load concentration directly under the nose altered the projectile trajectory in these cases. However, the depth-of-penetration increased and instability reduced with increased porosity and showed a considerable reduction in the affected penetration zone size. Even though there was less lateral motion due to the slower wave speed and dispersion, the stability increased due to the lesser resistance to penetration at higher porosity. As seen from these parametric variation simulations, projectile penetration in granular media is a complex, coupled phenomena dependent on many factors.

Our simulations clearly demonstrate that the instability increased due to the presence of friction as opposed to the frictionless case. The simulations also suggest that an increase in the randomness of the sand particle system will increase the inhomogeneous, unbalanced forces on the projectile increasing its instability. Even though the friction coefficient of 0.3 was constant in most simulations, it would increase with randomness due to the presence of random polyhedrons and random contact ensuing immediately after shock loading. On the contrary, the frictionless case removed this randomness resulting in balanced forces and more stable penetration. This was shown by more symmetric mushrooming of the projectile for the frictionless case.

The simulations showed that the finite and increasing magnitude of the displacement of the center-of-mass and rotational momentum coupled with the visual inspection of the projectile state at one body length of penetration could be used to predict the instability and trajectory change. The frictional case predicted the most unstable penetration leading to a significant trajectory change, of about 450, when the simulation was extended well beyond one body length of penetration.

The computations presented here represent an important start on a challenging problem. Although phenomena involving thermal effects and material fragmentations have been neglected in the present calculations, our results have provided a mechanistic explanation of the projectile

---



instability and trajectory change observed in penetration experiments. Parametric variations considered in our simulations have provided insight into how different physical features of the target affect projectile penetration.

#### **4.0 PERSONNEL SUPPORTED**

Individuals that have been involved in this project include:

- Conrad W. Felice (PI), Research Professor, Institute for Shock Physics, Washington State University
- Y. M. Gupta (co-PI), Professor, Institute for Shock Physics, Washington State University
- Sunil K. Dwivedi: Research Engineering Scientist, Institute for Shock Physics, Washington State University
- Lin Pei: Post-doctoral Research Associate, Institute for Shock Physics, Washington State University
- Russ Teeter: Graduate Student, Washington State University
- James Fernandez: Undergraduate, Washington State University

#### **5.0 PUBLICATION AND PRESENTATIONS**

During the period of this award, the PIs on this grant published the following works and delivered presentations relevant to the project.

Dwivedi, S. K., Teeter, R. D., Felice, C. W., and Gupta, Y. M., 2008. "Two Dimensional Mesoscale Simulations of Projectile Instability during Penetration in Dry Sand," *Journal of Applied Physics*, 104, 083502.

Teeter, R. D., S.K. Dwivedi, C. W. Felice, and Y. M. Gupta. 2007. "Mesoscale Simulations of Projectile Penetration into Sand," SHOCK07 Meeting of The American Physical Society, Hawaii, July.

Felice, C. W., 2007, "Particulate Mechanics," Keynote address at the Air Force Office of Scientific Research Workshop on Particulate Mechanics in Extreme Environments, University of Florida Research & Engineering Education Facility, Shalimar, Florida, January 23-25.

---



## 6.0 CHANGE IN AFOSR PROGRAM MANAGER

Dr. David S. Stargel

Program Manager

AFOSR/RSA

Air Force Office of Scientific Research Aerospace, Chemical, and Material Sciences

875 N. Randolph Street

Suite 325, Room 3112

Arlington VA, 22203-1768

## 7.0 REFERENCES

1. R. D. Teeter, S. K. Dwivedi, and Y. M. Gupta, *ISP-SAND: Theory Manual for the Creation of Sand Targets*, Institute for Shock Physics, Washington State University, Pullman, WA 99164-2816.
  2. R. D. Teeter, *Two Dimensional Mesoscale Simulations of Projectile Instability During Penetration in dry Sand*, MS Thesis, School of Mechanical and Materials Engineering, Washington State University, Pullman, WA.
  3. A. Okabe, *Spatial Tessellations: Concepts and Applications of Voronoi Diagrams* Wiley, Chichester; New York (2000).
  4. D. H. Krinsley, and J. C. Doornik, *Atlas of Quartz Sand Surface Textures*, Cambridge University Press, (1973).
  5. W. C. Mahaney, *Atlas of Sand Grain Surface Textures and Applications*, Oxford University Press, (1973).
  6. *CUBIT Mesh Generation Environment Volume 1: Users Manual*; Sandia National Laboratory, Report No. SAND94-1100.
  7. S. K. Dwivedi, *ISP-PREP: Preprocessor for the 2D Finite Element Simulation of the Plate Impact Material Property Experiment*, Institute for Shock Physics, Washington State University, Pullman, WA (in preparation).
  8. S. K. Dwivedi, J. R. Asay, and Y. M. Gupta, *Journal of Applied Physics*, 100, p. 083509 (2006).
  9. S. K. Dwivedi and Y. M. Gupta, *ISP-TROTP: 2D SMP Parallel Finite Element Code for Mesoscale Simulations*, Institute for Shock Physics, Washington State University, Pullman, WA (in preparation).
  10. J. M. Winey, R. Feng, and Y. M. Gupta, *Isotropic Material Models for the Elastic Response of Sapphire and Quartz Single Crystals Under Shock Wave Loading*, Institute for Shock Physics Internal Report, Washington State University, Pullman, WA, 2001.
  11. S. K. Dwivedi, J. L. Ding, and Y. M. Gupta, *International Journal of Computational Methods*, 2, 3, p. 341 (2005).
  12. C. H. M. Simha, and Y. M. Gupta, *Journal of Applied Physics*, 96, p. 1880 (2004).
  13. R. B. Boulet, and C. W. Young, *Deep Earth Penetration Technology (DEPT)*, U.S. Air Force Research Laboratory, Albuquerque, 1999.
-